ELSEVIER

The mechanical properties of solidified polyethylene glycol 600, an analog for lava crust

S.A. Soule *, K.V. Cashman

Department of Geological Sciences, University of Oregon, 1272 University of Oregon, Eugene, OR 97403-1272, USA

Abstract

The strength of lava crust and the role of that crust in determining lava flow dynamics and morphology are of fundamental importance in modeling lava flow behavior. Great improvements to flow models have been made by combining theoretical analysis with the results from analog experiments using polyethylene glycol (PEG 600) wax, which solidifies just below room temperature and can be used to simulate solidifying flows. However, a paucity of experimental data on the mechanical properties of solid PEG 600 has limited the quantitative interpretation of the role of crust in these experiments. We have, therefore, conducted experiments to measure the mechanical properties (tensile strength, shear strength, and Young's modulus) of solidified PEG 600 at temperatures and strain rates similar to those employed in analog experiments. The mechanical properties of PEG 600 can be modeled by a power law function of temperature, with the tensile strength exhibiting an additional dependence on strain rate. At intermediate temperatures, marked changes in the temperature dependence of the Young's modulus and in the character of failure surfaces indicate a transition from brittle to ductile behavior. We find that the strength of solid PEG 600 at experimental temperatures and strain rates exceeds that inferred for the crust on active laboratory flows by four orders of magnitude. This discrepancy is best explained by the presence of a thin visco-elastic layer separating the solid surface from the fluid interior of PEG 600 flows, a model that has been suggested to explain the behavior of some basaltic lava flows.
© 2003 Elsevier B.V. All rights reserved.

Keywords: lava flow; crust; PEG 600; rheology; tensile strength

1. Introduction

Crust is an important parameter of lava flow emplacement that is both effected by and affects physical processes during flow. For example, the rate of heat loss from crusted and crust-free lava differs dramatically (Crisp and Baloga, 1990, 1994), resulting in unique thermal (and resulting rheological) histories for lava transport systems with or without continuous surface crusts. However, complex feedback mechanisms among rates of flow cooling, crystallization, and flow advance rate directly influence the mechanical stability of the crust. Understanding these complexities have required that careful observations of active flows be supplemented by analog experiments performed under controlled conditions (e.g. Hulme,

---

* Corresponding author. Tel.: +1-541-346-5987;
Fax: +1-541-346-4692.
  E-mail addresses: ssoule@gladstone.uoregon.edu
(S.A. Soule), cashman@oregon.uoregon.edu (K.V. Cashman).

1974; Blake, 1990; Fink and Griffiths, 1990, 1992, 1998; Stasiuk et al., 1993; Griffiths and Fink, 1992a,b, 1993, 1997; Griffiths, 2000; Blake and Bruno, 2000). Many of these simulations have used polyethylene glycol (PEG 600) as an analog to lava because it freezes near room temperature (19–20°C) and can thus be used to investigate solidifying flows. However, the physical properties of solidified PEG 600 are poorly understood, limiting interpretation of the nature and role of the crust in flow emplacement. Here we present experimental measurements of the tensile strength, shear strength and Young's modulus of solid PEG 600 at temperatures (4–13°C) and strain rates (0.005–0.05 s^{-1}) relevant to PEG 600 flow experiments. We then use the results to constrain the role of solid crust in flow emplacement, both in the laboratory and, by inference, in lava flows and domes.

It has long been recognized that morphologic and dynamic differences among basaltic lava flow types can be related to variations in the rheology of flow interiors and the strength and thickness of surface crusts. Dana (1849, 1888) first interpreted 'a'a formation to result from solidification and subsequent crustal breakage at the flow front and hypothesized that the size of 'a'a clinkers reflected the thickness of the cooled crust at the time of their genesis. Since then, numerous studies have addressed the relative importance of crustal strength and internal flow rheology in the development of different surface morphologies and emplacement styles. Flow crusts may deform by ductile folding (Fink and Fletcher, 1978; Fink, 1980; Gregg et al., 1998) or brittle failure at length scales that reflect both the lava rheology and the thickness of the thermal boundary layer at the time of failure (e.g. Wentworth and Macdonald, 1953; Rowland and Walker, 1987; Cashman et al., 1999), resulting in a spectrum of surface morphologies from smooth pahoehoe to blocky lava flows. Kilburn (1981, 1990, 1993, 1996) has generalized flow models to argue that the distinct flow advance styles of pahoehoe and 'a'a are determined by rates of crustal growth vs. rates of crustal disruption, with 'a'a crusts experiencing near continuous failure and pahoehoe crusts failing episodically.

While the definition of crust is commonly mechanical (e.g. Wright and Okamura, 1977), changes in the mechanical properties of solidifying lava are directly linked to temperature and consequently the thermal structure and history of a lava flow. For this reason, models linking flow dynamics to cooling rates predict many aspects of flow morphology using a single dimensionless parameter, Ψ, which represents the relative importance of quenching and advection timescales (Fink and Griffiths, 1990, 1992; Griffiths and Fink, 1993). Also important, however, are both the rheology of the fluid interior (Hulme 1974; Griffiths and Fink, 1998; Cashman et al., 1999) and the development of a visco-elastic boundary layer between the fluid interior and brittle surface (Hon et al., 1994). For this reason, we use our measurements to examine the relative importance of these three thermo-mechanical layers during flow emplacement.

2. Methods

2.1. PEG 600

Polyethylene glycol is a crystalline, thermoplastic, water-soluble polymer that is commercially available in a wide range of molecular weights depending on the number of monomers (n),

$$OH - (-CH_2 - CH_2 - O-)_n - H,$$
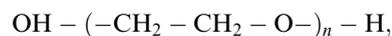
in the polymeric chain (Bailey and Koleske, 1976). This study uses PEG 600 (commercially produced as Carbowax 600 by the Union Carbide Corp.), the same material used in prior lava flow simulations (e.g. Fink and Griffiths, 1990; Blake and Bruno, 2000; Gregg and Fink, 2000). PEG has numerous industrial applications and as a result, a significant body of literature exists on the material. However, most studies are restricted to the properties of liquid, not solid, PEG (see Harris and Zalipsky, 1997 for a review). Measurements of the mechanical properties solid PEG exist only for compounds with molecular weights much greater than those used in flow experiments (PEG $n > 4000$; Al-Nasassrah et al., 1997).

2.2. Sample preparation

We prepare PEG 600 samples by heating the wax above its solidification temperature (T_s) and casting it in molds of the desired shape. For tensile strength measurements, the mold consists of two polystyrene cocktail cups with bottoms removed, placed end-to-end and separated by a rubber o-ring (Fig. 1a). The o-ring, which is removed prior to testing, creates a necked region to be fractured with a known cross-sectional area. We allow filled molds to equilibrate to experimental temperatures for $\sim$12 h. The mold for direct shear tests is formed by two $\sim$15-cm lengths of polyvinyl chloride (PVC) pipe, again separated by a rubber o-ring (Fig. 1b). A 2.5-mm-deep thread cut on the inside of each pipe prevents the solid PEG 600 from sliding during the tests. Volume loss of the PEG 600 during freezing results in holes through the center of the cylinder that occa-

Fig. 1. Molds for (a) tensile tests and (b) shear tests are constructed from polystyrene cocktail cups and lengths of PVC pipe, respectively. Each is separated by a split rubber o-ring that creates a necked region of known cross-sectional area to be fractured. In shear molds, a thread cut on the inside of the PVC pipe prevents the wax from sliding.

sionally penetrated the necked fracture region. Hole formation is limited, but not eliminated, by insulating the tops of the cylinders during cooling. We discard test results for samples with extreme volume loss.

We determine the solidification temperature of the PEG 600 with a concentric cylinder viscometer. Temperature is decreased in 0.5°C increments until the viscosity increases dramatically (Fig. 2), indicating the onset of solidification. To ensure homogeneity in physical properties, we measure the freezing point of small amounts of the wax ($\sim$3 liters) prior to use, and discard the PEG 600 after one use.

2.3. The apparatus

We conduct tests within a thermally regulated chamber at temperatures of 4°C, 7°C, 10°C, and 13.3°C, nearly spanning the range of temperatures in PEG 600 flow experiments (e.g. Fink and Griffiths, 1990; Blake and Bruno, 2000). A DC servo motor with a linear actuator produces constant strain at rates of 0.005, 0.01, 0.03, and 0.05 s^{-1}, covering the range of strain rates achieved in simulations (Griffiths and Fink, 1993).

For tension, two split ring clamps with inner surfaces beveled to fit the taper of the cups hold samples in place below the servo motor. The bottom clamp is fixed to a superstructure and the top clamp hangs freely from the linear actuator (Fig. 3). As the motor pulls, the sample self-centers within the clamps, is stretched, and finally fails. A force meter constructed of oil-hardened tool steel measures the applied stress. A wheatstone bridge produces a potential proportional to the stress that is collected by computer at 0.01-s intervals. The temperature dependence of the resistors in the wheatstone bridge requires that the force meter be calibrated before each set of experiments.

We apply direct shear to the sample through a linear bearing attached to the servo motor. Cylindrical samples are secured in a sheath, one side of which is fixed to the superstructure, the other side of which is attached to the linear bearing (Fig. 4). As the motor pulls on the linear bearing, a shear stress is produced in the sample. The shear appa-
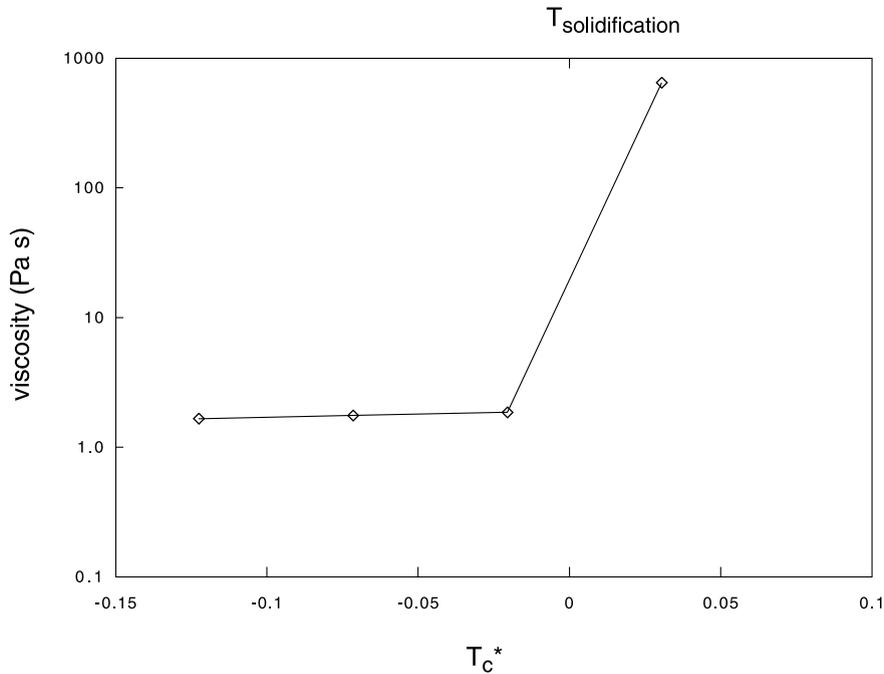
Fig. 2. Plot of viscosity vs. the complement of dimensionless temperature (T^*_c) for PEG 600. A sharp rise in viscosity is observed as the T^*_c approaches 0, the solidification temperature of the wax.

ratus was tested to ensure that no bending moment was applied to the samples.

3. Results

3.1. Tension

The ultimate tensile strength of a material (σ_{UTS}) is given (Jaeger and Cook, 1971) by the maximum tensile force (F_t) attained during a test to failure per unit cross-sectional area (a) of the sample,

$$\sigma_{UTS} = \frac{F_t}{a} \tag{1}$$

(Jaeger and Cook, 1971). At each temperature we conduct a minimum of five tests at each strain rate, spanning the range of the servo motor (cf. Section 2.3). Tests begin with an initial stress increase as the sample self-centers and locks into place. This is followed by a near-linear increase in stress until the yield point (σ_y) is reached. Achievement of the maximum tensile stress is pre-

ceded by a period of strain softening and followed by sample failure (Fig. 5). The ultimate tensile strength of solid PEG 600 (σ_{UTS}) increases systematically with decreasing temperature. Temperature is described by the complement of dimensionless temperature:

$$T^*_c = 1 - \frac{T}{T_s} \tag{2}$$

where temperature (T) and solidification temperature of the PEG 600 (T_s) are measured in degrees Celsius.

The increase in σ_{UTS} with decreasing temperature can be modeled as the power law relationship:

$$\sigma_{UTS} = C(T^*_c)^{1.25 \pm 0.04} \tag{3}$$

where strain rate (0.005, 0.01, 0.03, 0.05 s^{-1}) determines the constant C (1.46, 1.86, 2.08, and 2.38 MPa) (Fig. 6). This model correlates well with the data, with $R^2 = 0.98$ to 0.99 for each strain rate, and by definition, dictates that PEG 600 has no tensile strength at $T^*_c = 0$.
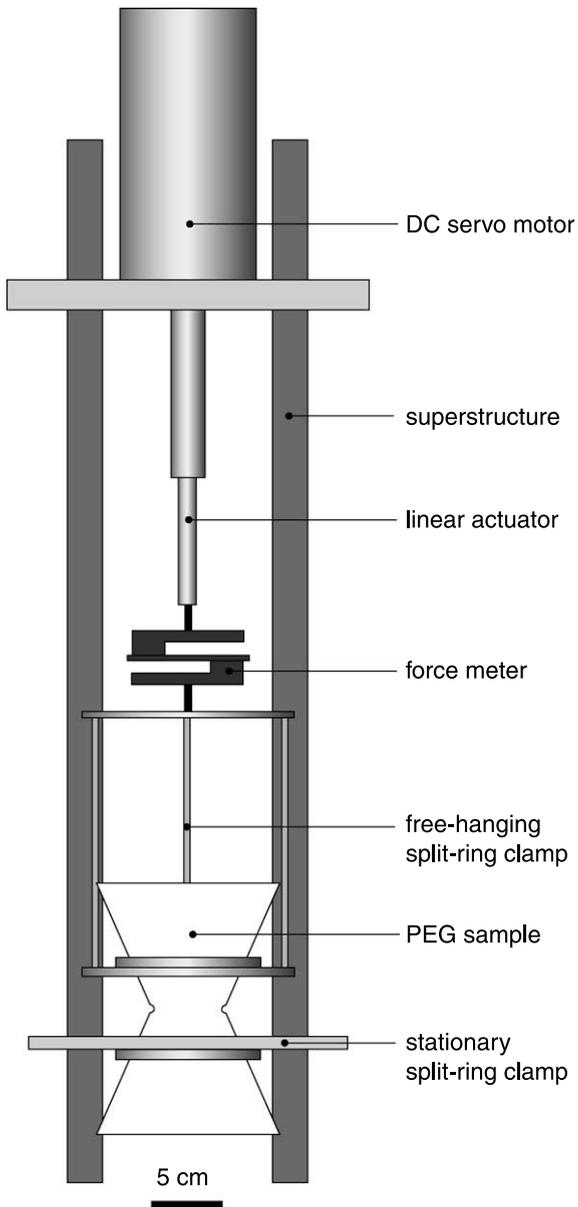
Fig. 3. Experimental apparatus for tensile tests. Samples are held in place by two split-ring clamps, the lower of which is fixed to a super structure. The upper clamp is in-line with the force meter and the servo motor. All tests are conducted within an isothermal environment.

A dependence of σ_{UTS} on strain rate ($\dot{\varepsilon}$) is observed in tensile tests at all temperatures and shows, on average, a 25% increase in σ_{UTS} from $\dot{\varepsilon} = 0.005$–$0.05$ s^{-1} (Fig. 7). This dependence can be modeled as the power law relationship:

$$\sigma_{UTS} = C(\dot{\varepsilon})^{0.19 \pm 0.01} \tag{4}$$

where the constant C (0.97, 1.80, 2.24, and 3.20 MPa) is determined by T^*_c (0.31, 0.48, 0.63, and 0.79). This dependence, while greater than anticipated for a purely elastic material, is often present in visco-elastic polymers (Ward, 1983). For time-dependent mechanical properties, increasing $\dot{\varepsilon}$ is equivalent to lowering temperature (Jaeger and Cook, 1971), which is consistent with our observations of greater σ_{UTS} at greater $\dot{\varepsilon}$ (Fig. 6).

3.2. Shear

We measure the ultimate shear strength of PEG 600 (σ_{USS}) at the same range of temperatures used in tensile tests. Initially tests were conducted at a range of strain rates, but as no detectable dependence on strain rate was observed, most shear strength tests were performed at $\dot{\varepsilon} = 0.01$ s^{-1}. Shear tests show an identical stress-strain evolution to tensile tests (Fig. 5).

The ultimate shear strength increases systematically with decreasing temperature (Fig. 8). The relationship is best fit ($R^2 = 0.953$) by the power law model:

$$\sigma_{USS} = C(T^*_c)^{0.44} \tag{5}$$

where C is a constant equal to 0.7 MPa. A linear model (dashed line) fits the data nearly as well ($R^2 = 0.938$), but defines a shear strength of 0.3 MPa at $T^*_c = 0$.

3.3. Young's modulus

For an idealized elastic material, the magnitude of externally applied stress (σ) below its yield point is proportional to strain (ε) by Hooke's Law:

$$\sigma = E \cdot \varepsilon \tag{6}$$

where the constant of proportionality (E) is the Young's modulus, a characteristic material property. The Young's modulus of solid PEG 600 is determined from the linear portion of the stress-strain curve in tensile tests (b to c in Fig. 5). In general, the Young's modulus is not a function of strain rate but is dependent on temperature. This
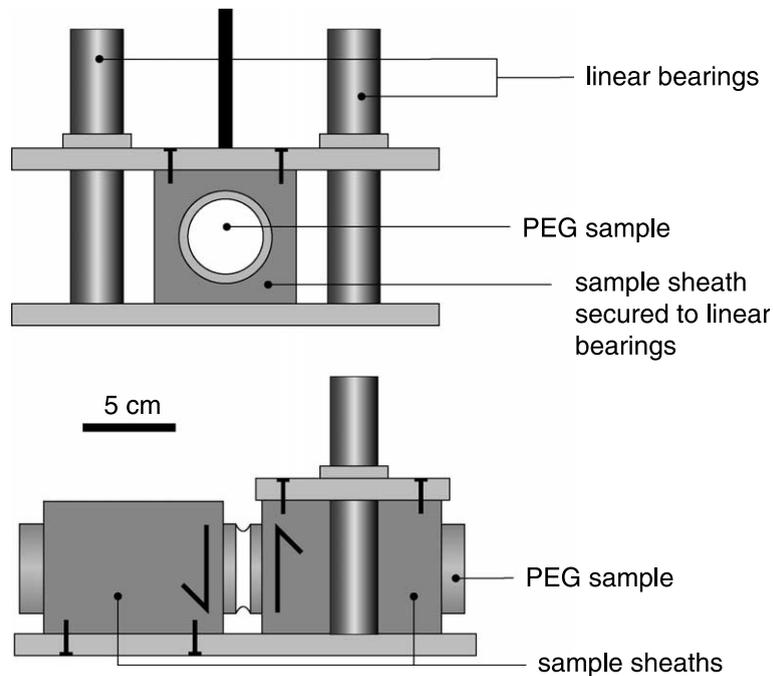
Fig. 4. Front view (top) and side view (bottom) of experimental apparatus for shear tests. Peg 600 cylinders are placed in sample sheaths, one of which is secured to a linear bearing. The other sample sheath is secured to a bottom plate that is in turn secured to the superstructure. An upward force on the former sample sheath, guided by the linear bearing, produces direct shear in the sample. All tests are conducted within an isothermal environment.

relationship is well characterized ($R^2 = 0.924$) by a power law model of the form:

$$E = C(T_c^*)^{0.40} \tag{7}$$

where C is a constant equal to 5.2 MPa (Fig. 9).

Although E shows no systematic strain rate dependence, tests at $T_c^* = 0.48$ show an abrupt increase in E between strain rates of 0.03 and 0.05 s^{-1} (Fig. 9). The Young's modulus at $T_c^* = 0.48$ and $\dot{\varepsilon} = 0.05$ s^{-1} is 4.7 MPa, approximately equal to the average E at $T_c^* > 0.5$. At strain rates of 0.01–0.03 s^{-1}, $E = 3.8$ MPa, and falls on the power law curve defined by the experiments at $T_c^* \leq 0.48$. This step-like increase at $T_c^* = 0.48$ and high strain rate reveals a threshold in T_c^*–$\dot{\varepsilon}$ space above which the deformation shows little or no temperature dependence.

3.4. Mode of failure

In tensile tests, the morphology of the PEG 600 failure surface varies with temperature (T_c^*) and
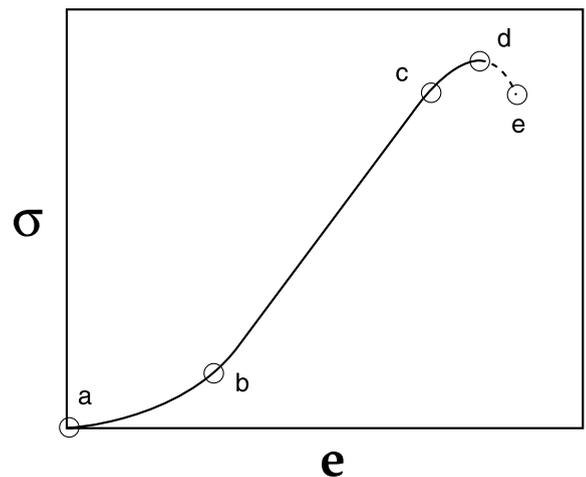
Fig. 5. A typical stress-strain curve for tensile and shear tests shows an initial increase in force (a–b) as the sample is locked into place. Stress then increases linearly (b–c) reflecting elastic deformation and allowing the determination of Young's modulus. After the yield point (c), a period of strain softening occurs during which the maximum tensile stress (d) is achieved. Brittle sample failure occurs at (d) and ductile sample failure occurs at (e).
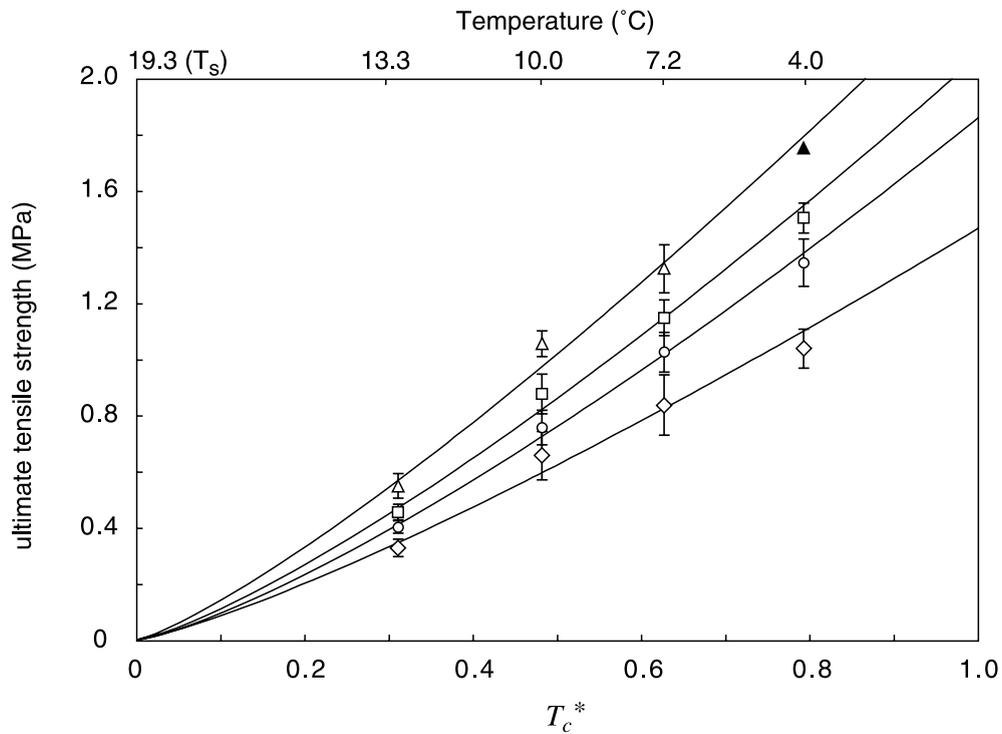
Fig. 6. Ultimate tensile stress (σ_{UTS}) increases systematically with increasing T^*_c. Strain rate ($\dot{\varepsilon}$) is indicated by symbol shape ($\diamond = 0.005$ s^{-1}, $\bigcirc = 0.01$ s^{-1}, $\square = 0.03$ s^{-1}, and $\triangle = 0.05$ s^{-1}). The symbol $\blacktriangle$ denotes an inferred tensile strength for tests that exceeded the capacity of the apparatus. Error bars show 95% confidence interval. Power law models fit to the data indicate no tensile strength at the solidification temperature.

strain rate ($\dot{\varepsilon}$). At high T^*_c and high $\dot{\varepsilon}$ PEG 600 shows discrete conchoidal fractures, with plumose structures indicating the location of fracture initiation (Fig. 10a). At low T^*_c and low $\dot{\varepsilon}$ the failure surface has a conical form that propagates through the necked region of the sample and has a roughness that suggests ductile extension rather than brittle fracture (Fig. 10b). At intermediate temperatures and strain rates the failure surface is mostly rough and irregular with some areas of smooth fracture. We have classified failure surfaces as type I (conical, rough failure surface), type II (a failure surface combining rough and conchoidal features), or type III (purely conchoidal fracture). Fig. 11 illustrates the location of the transitions between the three types as a function of T^*_c and $\dot{\varepsilon}$. The onset of type III fractures at $T^*_c = 0.48$ and strain rate of 0.03–0.05 s^{-1} is coincident with a dramatic increase in the Young's modulus (cf. Section 3.3).

4. Discussion

The influence of solid crust on PEG 600 flow mechanics is evidenced by changes in flow behavior with changes in cooling rate (Griffiths and Fink, 1993). Our experiments, which characterize the mechanical properties of solidified PEG 600 as a function of both temperature and strain rate, permit us to evaluate the role of solid PEG 600 in the emplacement of wax flows, and by analogy, the role of the brittle crust in lava flow emplacement. The measured strength of solid PEG 600 is much greater (by $\sim 10^4$) than the strength of PEG 600 flow crust that has been inferred from experiments by quantifying differences in the geometry of crusted and crust-free flows. To explain this discrepancy, we examine several models of the role of the crust in solidifying PEG 600 flows and natural flow examples.
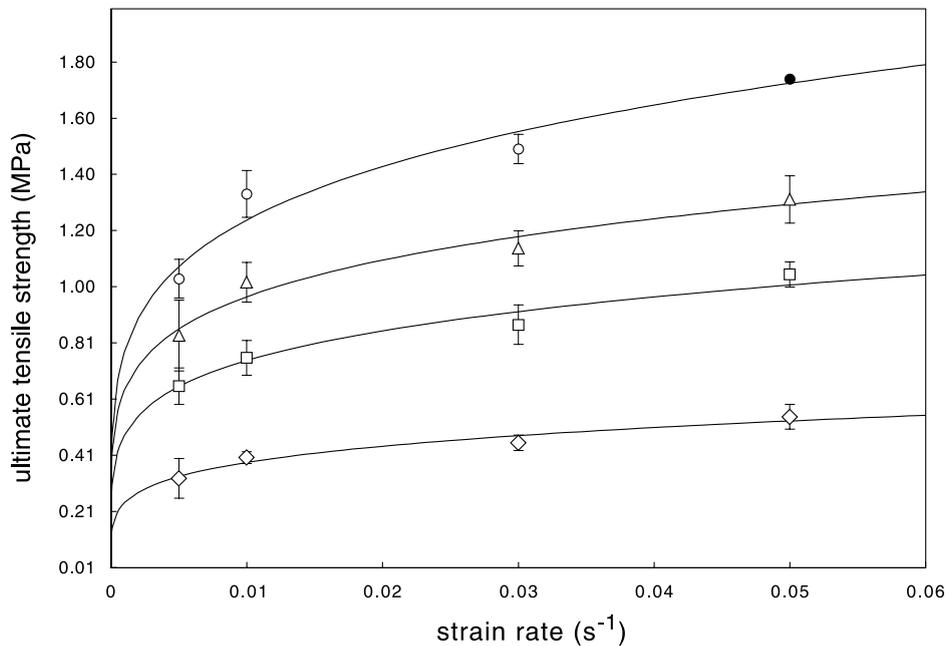
Fig. 7. Ultimate tensile stress (σ_{UTS}) increases systematically with increasing strain rate. T^*_c is indicated by symbol shape ($\diamond = 0.31$, $\bigcirc = 0.48$, $\square = 0.63$, and $\triangle = 0.79$). The symbol ● denotes an inferred tensile strength for tests that exceeded the capacity of the apparatus. Error bars show 95% confidence interval. Solid lines indicate power law models fit to the data.
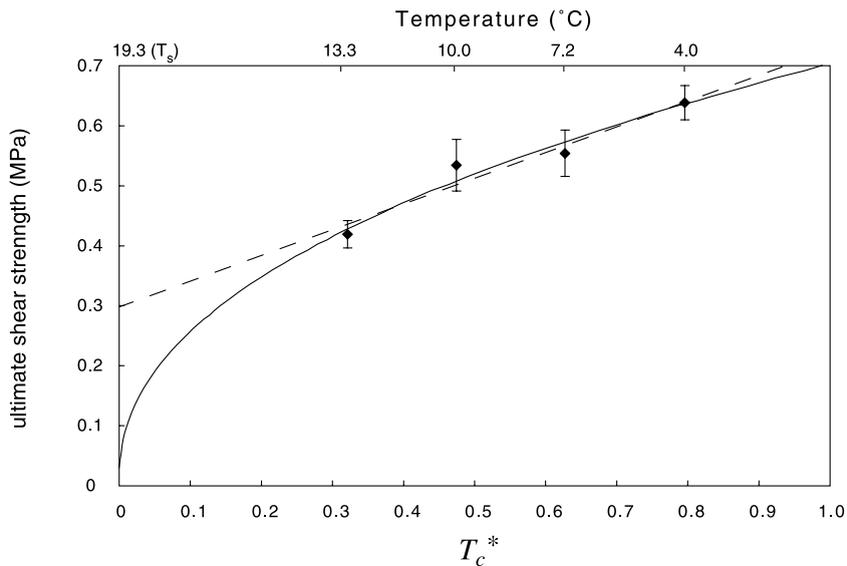
Fig. 8. Shear stress (σ_{USS}) increases systematically with T^*_c. Error bars indicate 95% confidence interval. The dashed line represents a linear model, which indicates a shear strength of ~ 0.3 MPa at the solidification temperature. The solid line represents the favored power law model.
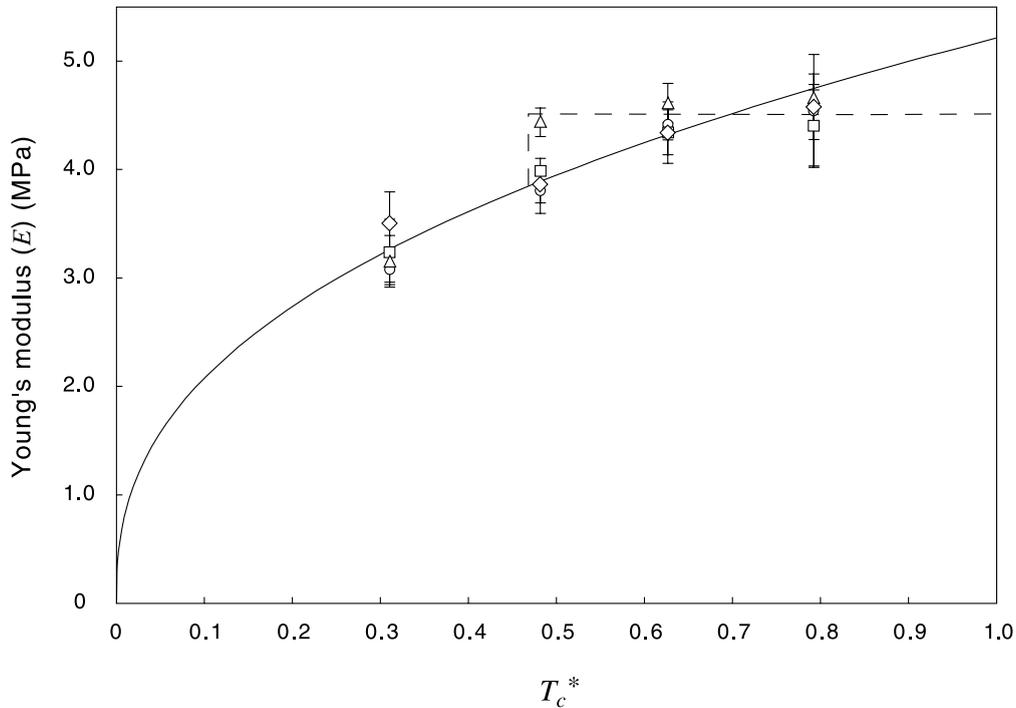
Fig. 9. Young's modulus (E) shown as a function of dimensionless temperature ($T*_c$) shows no systematic dependence on strain rate which is indicated by symbol shape (($\diamond$ = 0.005 s^{-1}, $\circ$ = 0.01 s^{-1}, $\square$ = 0.03 s^{-1}, and $\triangle$ = 0.05 s^{-1}). The solid line represents the power law model which fits E accurately at $T*_c < 0.5$ and reasonably well for E at $T*_c > 0.5$. The dashed lines indicates the location of a step-like increase in E at $T*_c \sim 0.5$ and $\dot{\varepsilon}$ = 0.05 s^{-1}, after which average E remains nearly constant.

4.1. Mechanical properties

Solidified PEG 600 increases in strength with decreasing temperature. Ultimate tensile strength (σ_{UTS}) is best modeled as a power law function of dimensionless temperature (T_c*) with $\sigma_{UTS} \propto T_c^{*\ 1.25\pm0.04}$. Tensile strength also shows a dependence on strain rate, although σ_{UTS} varies little over the order of magnitude $\dot{\varepsilon}$ increase in our experiments (cf. Section 3.1). Ultimate shear strength (σ_{USS}) and Young's modulus (E) can also be modeled as power laws with $\sigma_{USS} \propto T_c^{*\ 0.44}$ and $E \propto T_c^{*\ 0.40}$.

A power law dependence of mechanical properties on temperature is commonly observed as rocks approach their melting temperatures. Examples include the fracture strength of microgranodiorite (Murrell and Chakravarty, 1973) and the Young's modulus of olivine tholeiite (Ryan and Sammis, 1981). In the latter, a rapid decrease in E is observed as olivine tholeiite is heated through the glass transition temperature. In PEG 600, similar behavior in E is observed around $T*_c = 0.48$ (Fig. 9). At smaller $T*_c$, dE/dT_c is large, suggesting plastic behavior (i.e. ductile deformation), while at greater $T*_c$, dE/dT_c is small, suggesting elastic behavior (i.e. brittle deformation). Further evidence for a brittle–ductile transition is found in the onset of conchoidal fracture surfaces at the same temperature that marks the change in E ($T*_c = 0.48$) (Fig. 11).

Considering the combination of elastic and plastic deformation observed in solidified PEG 600, a suitable rheological model would be that of a Maxwell body with a characteristic Maxwell time (relaxation time) of:

$$\tau_m = \frac{\eta}{E}, \tag{8}$$

where η is the viscosity of the solidifying PEG 600 (Jaeger and Cook, 1971). At timescales greater than τ_m, the PEG 600 deforms plastically and at
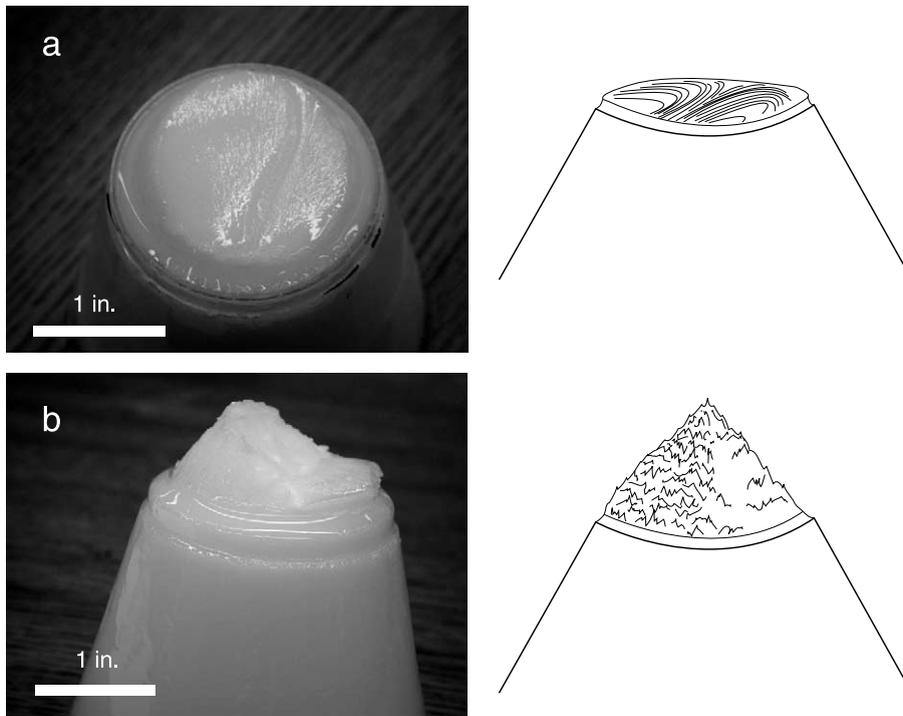
Fig. 10. At cooler temperatures and greater strain rates, PEG 600 fractures conchoidally (a) and shows plumose structures indicating the location of fracture initiation and is classified as type I. At warmer temperatures and lower strain rates, the failure surface has a conical form that penetrates through the necked region of the sample. The surface is rough and suggests ductile rather than brittle deformation and is classified as type III. A spectrum of failure surfaces that contain characteristics of both end members are classified as type II.

timescales below τ_m, it deforms elastically. Although difficulty in measuring η at high T^*_c and E at low T^*_c limit a quantitative assessment of τ_m, we can qualitatively constrain τ_m for solid PEG 600 based on our experiments. The inferred transition from elastic to plastic behavior at $T^*_c \sim 0.5$ and $\dot{\varepsilon} = 0.05$ s^{-1} suggests $\tau_m \sim 500$ s at this temperature. Purely elastic deformation at $T^*_c > 0.5$, implies that τ_m increases as the temperature decreases.

4.2. The role of solid PEG 600 in crust strength

The behavior of the two-component system of solid crust and molten PEG 600 is mechanically controlled by a balance between the forces driving flow (buoyancy) and the forces retarding flow from both the interior (e.g. viscosity) and from the crust. Of these, the retarding forces from the crust are the least understood. Griffiths and Fink

(1993) discuss three possibilities for the nature of the crustal retarding forces: (1) an effective Newtonian viscosity (η_c) much greater than that of the interior, (2) a plastic yield stress (shear strength), or (3) an elastic tensile strength (σ_c). By setting the buoyancy forces equal to each retarding force, imposing conservation of mass, and assuming scaling relationships for crustal growth and strain rate, it is possible to quantify the time-dependence of extrusion geometry expressed as radius (R) and depth (H) (see Griffiths and Fink, 1993 for derivations). Here we show solutions for buoyancy balanced by a Newtonian shear stress in the crust,

$$R(t) = \left[\frac{\rho g'}{\eta_c} \kappa^{-1/2} Q^3 t^{1/2(6\alpha+1)} \right]^{\frac{1}{7}} \tag{9}$$

$$H(t) = \left(\frac{\eta_c}{\rho g'} \right)^{2/7} (\kappa Q)^{1/7} t^{1/7(\alpha-1)} \tag{10}$$
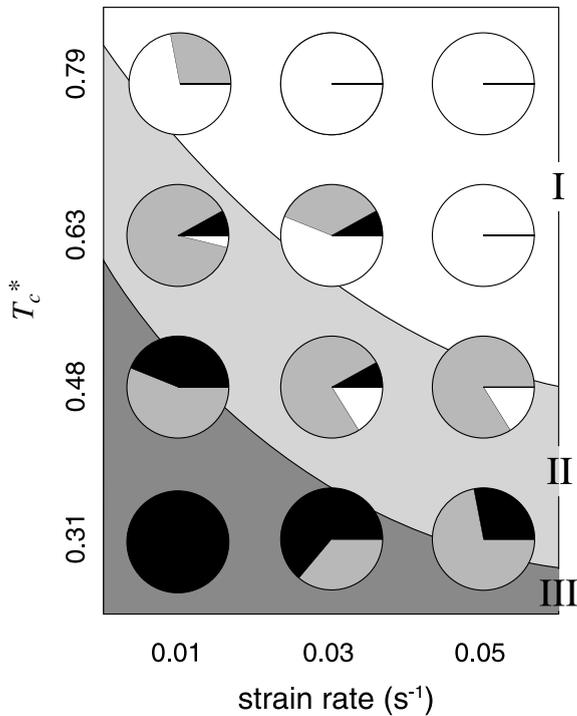
Fig. 11. PEG 600 failure surfaces change systematically with T^*_c and $\dot{\varepsilon}$. The fraction of failure surfaces of each type at a given T^*_c and $\dot{\varepsilon}$ are indicated by the proportion of color in the pie chart (black = type III, gray = type II, and white = type I). Fields of white, gray, and dark gray in the background suggest qualitative divisions between the dominant failure surface type.

and by a yield strength (either plastic shear or elastic tensile strength) in the crust,

$$R(t) = \left[\frac{\rho g'}{\sigma_c} \kappa^{-1/2} Q^2 t^{1/2(4\alpha - 1)} \right]^{\frac{1}{4}} \quad (11)$$

$$H(t) = \left(\frac{\sigma_c}{\rho g'} \right)^{1/2} (\kappa t)^{1/4} \quad (12)$$

(see Table 1 for description of terms). Differences in the time exponents are used to determine that buoyancy forces balanced by a yield strength in the crust (Eqs. 11 and 12) most accurately describe the observed changes in flow geometry (i.e. $R(t)$ and $H(t)$). This model can then be used to infer an effective shear or tensile strength (σ_c) in the crust of 40–100 Pa (Griffiths and Fink, 1993), more than four orders of magnitude lower

than the measured tensile strength of solidified PEG 600 (Fig. 6).

4.3. Crustal models

The discrepancy between the measured and inferred PEG 600 strengths can be explained in a number of ways. One explanation is that the crust, where failure occurs, is considerably thinner than predicted (Fig. 12a). In PEG 600 flow experiments, crust is assumed to thicken by 1-D heat conduction (proportional to $\sqrt{t}$; Griffiths and Fink, 1993) but crust may be modified due to deformation during flow (Gregg et al., 1998). We can test whether a thinned crust can account for the strength difference with a simplified, brittle-shell mechanical model that has been applied to lava dome growth by Iverson (1990). This model describes a static balance between buoyancy-driven flow and a continuous crust with known thickness and tensile strength. Using our measured tensile strength of solid PEG 600 and crust thickness of 1–10 mm observed in PEG 600 experiments (Fink and Griffiths, 1990), this model

Table 1
Symbols used

σ	stress (Pa)
F_t	tensile force (N)
σ_c	effective crust strength (Pa)
σ'_t	tensile stress at crack tip (Pa)
σ_{UTS}	ultimate tensile strength (Pa)
σ_{USS}	ultimate shear strength (Pa)
σ_y	yield point (Pa)
ε	strain
$\dot{\varepsilon}$	strain rate (s^{-1})
E	Young's modulus (Pa)
T	temperature (°C)
T_s	solidification temperature (°C)
T^*_c	complement of dimensionless temperature
η_c	viscosity of the crust (Pa s)
a	cross-sectional area (m^2)
r	radius of curvature (m)
c	crack length (m)
t	time (s)
Q	effusion rate (m^3 s^{-1})
H	extrusion height (m)
R	extrusion radius (m)
κ	emissivity (m^2 s^{-1})
g	gravity (ms^{-2})
ρ	density (kg m^{-3})
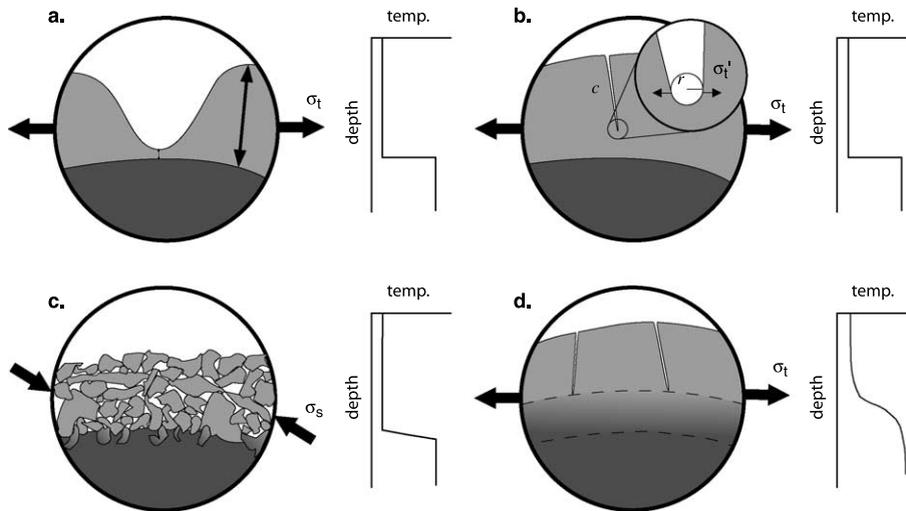
Fig. 12. Four models explaining the difference between the inferred strength of PEG 600 crust and the empirical strength of solid PEG 600 are shown schematically with liquid PEG 600 indicated by dark gray and solid PEG 600 by light gray. Arrows indicated direction of tensile and shear stresses. The four models are a thinned, but continuous crust (a), a cracked crust (b), a layer of solid PEG 600 pieces (c), and a thin visco-elastic layer underlying a cracked solidified crust (d). To the right of each model is a temperature profile through the thermal boundary layer.

predicts dome heights of 0.5–1.5 m, heights that greatly exceed those observed in experimental PEG 600 flows (0.01–0.1 m; Fink and Griffiths, 1990, 1992; Griffiths and Fink, 1993). For these observed flow heights, this model predicts a static balance with a crust $\sim 4 \times 10^{-5}$–4×10^{-7} m thick, too thin to be considered reasonable.

The crust of both analog and natural flows is generally fractured (e.g. Fink and Griffiths, 1992; Anderson et al., 1998), which will affect crust strength. In mechanical tests, small (sub-microscopic) flaws can reduce the functional strength of glass, another brittle, homogenous material, by up to three orders of magnitude (Scholze, 1990). This strength decreases results from stress concentration at crack tips, a phenomenon recognized by A.A. Griffiths in the early 1900's and formalized by Inglis (1913) as:

$$\sigma'_t = 2\sigma_t \left(\frac{c}{r}\right)^{\frac{1}{2}} \tag{13}$$

where σ'_t is the tensile stress at the crack tip, σ_t is applied tensile stress, c is crack length, and r is radius of curvature (Fig. 12b). Eq. 13 predicts a two order of magnitude increase in tensile stress at the crack tip over the applied tensile stress for a

2-mm-long crack with a 50-μm radius of curvature. However, a crack would have to be either unreasonably long (> 10 cm) or unreasonably narrow ($< 5.0 \times 10^{-11}$ m) to account for the observed 10^4 difference between measured and inferred strength. Thus, while stress concentration at crack tips may play a role in crustal failure, it cannot by itself explain the observed strength discrepancy.

Although individual fractures decrease solid strength, flow surfaces may be so fractured that the strength of individual crustal fragments plays no role in flow emplacement except thermal insulation. If the crust were composed of a collection of discrete, solid fragments its strength would arise from cohesion between the fragments (Fig. 12c; Griffiths and Fink, 1993; Fink and Griffiths, 1998), a phenomenon most likely to be important at the edges of flows and domes where piles of talus collect. Although our experiments cannot be used to address this model, it seems unlikely that this mechanism can explain the observed strength difference for all flows. For example, experiments performed under laminar flow conditions still exhibit retarding forces from the crust despite the absence of abundant crustal fragments

(Fink and Griffiths, 1990; Blake and Bruno, 2000).

Finally, where the crust (fractured or continuous) is connected to the molten interior by a visco-elastic layer, the rheological properties of this intermediate layer may dominate the emplacement process (Hon et al., 1994). In this model, a partially solidified sub-surface layer controls the flow dynamics, and observed brittle behavior in the crust occurs as a passive response to deformation of this visco-elastic layer (Fig. 12d). An appealing aspect of the visco-elastic layer model is that it acknowledges a continuous temperature profile through the mechanical and thermal boundary layer.

The presence of a visco-elastic layer can be used to reconcile differences in the inferred and measured PEG 600 strengths if we extrapolate our strength measurements to temperatures near the solidification temperature ($T^*_c = 0$) of the PEG 600. Tensile and shear strengths approach the values inferred from experiments (40–100 Pa, Griffiths and Fink, 1993; 10–15 Pa, Blake and Bruno, 2000) at temperatures of 19–19.5°C depending on the T_s of the PEG 600. At such low T^*_c (0.001–0.01), crust thickness and strength would be very sensitive to the solidification temperature (T_s), which can vary among batches of PEG 600. This may explain the order of magnitude difference in PEG 600 flow crust strength inferred from the experiments of Griffiths and Fink (1993) and Blake and Bruno (2000). Our analysis indicates that PEG 600 would have a very long τ_m at these temperatures ($\gg 500$ s), and thus would deform plastically at the range of strain rates achieved in flow experiments (0.001–0.01 s^{-1}; Griffiths and Fink, 1993).

Failure can still occur within the plastic regime as evidenced by our experiments at $T^*_c < 0.5$. On a molecular level, plastic failure of the PEG 600 results from stretching of individual polymeric chains beyond either their stress or strain limit (Ward, 1983). Macroscopically, when the rate of chain breakages becomes large enough, a rupture propagates and sample failure occurs. Consequently, the strength of this visco-elastic layer is directly related to the tensile strength of the individual polymeric chains, a property that will vary with temperature and strain rate (Bueche, 1955) as observed in our experiments.

The four models described above – involving thinned crust, cracked crust, crustal fragments, and sub-surface visco-elastic layer – can be used to explain the observed difference in the strength of crust inferred from PEG 600 flow experiments and the measured strength of solidified PEG 600. The first three models rely on a purely mechanical definition of the crust. Thinned and cracked crusts fail to adequately explain the difference. Cohesive strength in a layer of crustal fragments cannot be ruled out for many flow types, but does not explain the discrepancy for flows with largely continuous crusts. The final model, a sub-surface, visco-elastic layer, recognizes both mechanical and thermal definitions of the crust. Such a layer would deform plastically, but would still fail at stresses equivalent to those inferred from flow experiments.

4.4. Application to lava flows

Hon et al. (1994) suggested that a visco-elastic layer provides the strength that allows the inflation of pahoehoe flows. The top of the visco-elastic layer is identified by incandescent lava (~ 800°C) that cannot be penetrated by brittle fractures in the solid crust (Hon et al., 1994). The base of the visco-elastic layer is identified by a transition from lava with a finite strength to lava without strength, and has been observed in Hawaiian lava lakes at $T = 1070$°C (Wright and Okamura, 1977). In addition to its ability to constrain the lateral advance of lava, this layer is able to maintain overpressures of ~ 1 bar within the flow core, as evidenced by elevated dissolved volatiles and low vesicularity in breakouts from the primary flow (Hon et al., 1994) and excessive decreases in vesicularity beneath the flow surface (Cashman and Kauahikaua, 1997).

While the presence of a visco-elastic layer was identified on pahoehoe flows, the applicability of this model extends to 'a'a flows as well. Stalled 'a'a flow fronts will often rupture allowing fluid lava to escape. Dragoni and Tallarico (1996) model the timing of this failure by considering a visco-elastic layer at the base of the brittle crust

that deforms ductiley before failure in response to pressure from the hydraulic head of the fluid lava core. Assumed rheological properties of the visco-elastic layer partially solidified basalt suggest times of 24–72 h to accumulate excess stresses in the crust, times that are broadly consistent with those observed for failure of Etnean ′a′a flow fronts (Pinkerton and Sparks, 1976). By definition, a sub-surface, visco-elastic layer should be present on all types of lava flows that display surface crusts, and the examples described above show that it can account for many aspects of flow emplacement.

5. Conclusions

Experiments on solidified PEG 600 reveal temperature-dependent mechanical properties that are best described by power law models. A transition between ductile and brittle behavior of PEG 600 at a dimensionless temperature (T^*_c) of ~ 0.5 and strain rate of 0.05 s^{-1} is evidenced by a change in the dominant fracture style from type I to III and a step-like increase in Young's modulus (E) that yields a relaxation time of ~ 500 s. The relaxation time is an inverse function of temperature.

The strength of the PEG 600 flow crust inferred from analog experiments is four orders of magnitude smaller than the measured strengths. We can reconcile the strength discrepancy between measured PEG 600 strength and inferred crustal strength by the presence of a thin visco-elastic layer beneath the brittle crust (e.g. Hon et al., 1994) that is capable of retarding flow. Near the solidification temperature PEG 600 is well within the observed field of ductile deformation. Ductile failure, controlled by the strength of polymeric chains, is sensitive to both temperature and strain rate, as has been observed in PEG 600 flow experiments. Brittle deformation observed in the crust of analog experiments and natural flows is a passive expression of deformation and failure of the underlying visco-elastic layer. While the presence of a visco-elastic layer has been used to explain the emplacement of pahoehoe and ′a′a flows, results of PEG 600 dome emplacement experiments (Griffiths and Fink, 1993) suggest

that this model may apply to more silicic flows as well.

References

Al-Nasassrah, M.A. et al., 1997. The effect of an increase in chain length on the mechanical properties of polyethylene glycols. Eur. J. Pharm. Biopharm. 46, 31–38.

Anderson, S.W. et al., 1998. Block size distributions on silicic lava flow surfaces: Implications for emplacement conditions. Geol. Soc. Am. Bull. 110, 1258–1267.

Bailey, F.E., Koleske, J.V., 1976. Poly(ethylene) Oxide. Academic Press, New York.

Blake, S., 1990. Viscoplastic models of lava domes. In: Fink, J.H. (Eds.), Lava Flows and Domes: Emplacement Mechanisms and Hazard Implications. Springer, Berlin.

Blake, S., Bruno, B.C., 2000. Modeling the emplacement of compound lava flows. Earth Planet. Sci. Lett. 184, 181–197.

Bueche, F., 1955. Tensile strength of plastics above the glass temperature. J. Appl. Phys. 26, 1133–1140.

Cashman, K.V., Kauahikaua, J.P., 1997. Reevaluation of vesicle distributions in basaltic lava flows. Geology 25, 419–422.

Cashman, K.V. et al., 1999. Cooling and crystallization of lava in open channels, and the transition of pahoehoe lava to ′a′a. Bull. Volcanol. 61, 306–323.

Crisp, J., Baloga, S., 1990. A model for lava flows with two thermal components. J. Geophys. Res. 98, 1255–1270.

Crisp, J., Baloga, S., 1994. Influence of crystallization and entrainment of cooler material on the emplacement of basaltic aa lava flows. J. Geophys. Res. 99, 11819–11831.

Dana, J.D., 1849. Geology: United States Exploring Expedition, vol. 10. Putnam, New York.

Dana, J.D., 1888. History of the changes in the Mt. Loa craters, on Hawai′i. Am. J. Sci. 35, 15–34, 213–228, 282–289 and 36, 14–32, 81–112, 167–175.

Dragoni, M., Tallarico, A., 1996. A model for the opening of ephemeral vents in a stationary lava flow. J. Volcanol. Geotherm. Res. 74, 39–47.

Fink, J.H., Fletcher, R.C., 1978. Ropy pahoehoe; surface folding of a viscous fluid. J. Volcanol. Geotherm. Res. 4, 151–170.

Fink, J.H., 1980. Surface folding and viscosity of rhyolite flows. Geology 8, 250–254.

Fink, J.H., Griffiths, R.W., 1990. Radial spreading of viscous-gravity currents with solidifying crust. J. Fluid Mech. 221, 485–509.

Fink, J.H., Griffiths, R.W., 1992. A laboratory analog study of the surface morphology of lava flows extruded from point and line sources. J. Volcanol. Geotherm. Res. 54, 19–32.

Fink, J.H., Griffiths, R.W., 1998. Morphology, eruption rates and rheology of lava domes; insights from laboratory models. J. Geophys. Res. (B) 103, 527–545.

Gregg, T.K.P., Fink, J.H., Griffiths, R.W., 1998. Formulation of multiple fold generations on lava flow surfaces: Influence of strain rate, cooling rate, and lava composition. J. Volcanol. Geotherm. Res. 80, 281–292.

Gregg, T.K.P., Fink, J.H., 2000. A laboratory investigation into the effects of slope on lava flow morphology. J. Volcanol. Geotherm. Res. 96, 145–159.

Griffiths, R.W., Fink, J.H., 1992a. Solidification and morphology of submarine lavas: A dependence on extrusion rate. J. Geophys. Res.. 97, 19729–19737.

Griffiths, R.W., Fink, J.H., 1992b. The morphology of lava flows in planetary environments: Predictions from analog experiments. J. Geophys. Res. 97, 19739–19748.

Griffiths, R.W., Fink, J.H., 1993. Effects of surface cooling on the spreading of lava flows and domes. J. Fluid Mech. 252, 667–702.

Griffiths, R.W., Fink, J.H., 1997. Solidifying bingham extrusions; a model for the growth of silicic lava domes. J. Fluid Mech. 347, 13–36.

Griffiths, R.W., 2000. The dynamics of lava flows. Ann. Rev. Fluid Mech. 32, 477–518.

Harris, J.M., Zalipsky, S., 1997. Poly(ethylene glycol) Chemistry and Biological Applications. American Chemical Society, Washington, DC.

Hon, K. et al., 1994. Emplacement and inflation of pahoehoe sheet flows: Observations and measurements of active lava flows on Kilauea Volcano, Hawai'i. Geol. Soc. Am. Bull. 106, 351–370.

Hulme, G., 1974. The interpretation of lava flow morphology. Geophys. J. R. Astron. Soc. 39, 361–383.

Inglis, C.E., 1913. Stresses in a plate due to the presence of cracks and sharp corners. Trans. Inst. Naval Archit. 55, 219.

Iverson, R.M., 1990. Lava domes modeled as brittle shells that enclose pressurized magma, with application to Mount St. Helens. In: Fink, J.H. (Eds.), Lava Flows and Domes: Emplacement Mechanisms and Hazard Implications. Springer, Berlin.

Jaeger, J.C., Cook, N.G.W., 1971. Fundamentals of Rock Mechanics. Chapman and Hall, London.

Kilburn, C.R.J., 1981. Pahoehoe and aa lavas: A discussion and continuation of the model of Peterson and Tilling. J. Volcanol. Geotherm. Res. 11, 373–382.

Kilburn, C.R.J., 1990. Surfaces of aa flow-fields on Mount Etna, Sicily; morphology, rheology, crystallization and scaling phenomena. In: Fink, J.H. (Eds.), Lava Flows and Domes: Emplacement echanisms and Hazard Implications. Springer Verlag, Berlin.

Kilburn, C.R.J., 1993. Lava crusts, aa flow lengthening and the pahoehoe–aa transition. In: Kilburn, C.R., Luongo, G. (Eds.), Active Lavas. UCL Press, London.

Kilburn, C.R.J., 1996. Patterns and predictability in the emplacement of subaerial lava flows and flow fields. In: Scarpa, R., Tilling, R.I. (Eds.), Monitoring and Mitigation of Volcano Hazards. Springer, Berlin.

Murrell, S.A.F., Chakravarty, S., 1973. Some new rheological experiments on igneous rocks at temperatures up to 1120°C. Geophys. J. R. Astron. Soc. 34, 211–250.

Pinkerton, H., Sparks, R.S.J., 1976. The 1975 sub-terminal lavas, Mount Etna: A case history of the formation of a compound lava field. J. Volcanol. Geotherm. Res. 1, 167–182.

Rowland, S.K., Walker, G.P.L., 1987. Toothpaste lava: Characteristics and origin of a lava structural type transitional between pahoehoe and aa. Bull. Volcanol. 49, 631–641.

Ryan, M.P., Sammis, C.G., 1981. The glass transition in basalt. J. Geophys. Res. 86, 9519–9535.

Scholze, H., 1990. Glass: Nature, Structure, and Properties. Springer, New York.

Stasiuk, M.V., Jaupart, C., Sparks, R.S.J., 1993. Influence of cooling on lava-flow dynamics. Geology 21, 335–338.

Ward, I.M., 1983. Mechanical Properties of Solid Polymers. Wiley, Chichester.

Wentworth, C.K., Macdonald, G.A., 1953. Structures and forms of basaltic rocks in Hawai'i. U.S. Geol. Surv. Bull. 994, 98 pp.

Wright, T.L., Okamura, R.T., 1977. Cooling and Crystallization of Tholeiitic Basalt, 1965 Makaopuhi Lava Lake, Hawai'i. U.S. Geol. Surv. Prof. Pap. 1004, 78 pp.